Theory of Electrophoretic Separations

Part II: Construction of a Numerical Simulation Scheme and Its Applications

The mathematical model outlined in Part I is recast in a form suitable for numerical computation. The spatial derivatives are replaced by finite-difference expressions, which leads to a set of ordinary differential equations coupled to a set of nonlinear algebraic relations. This system is solved using existing integration techniques. The resulting algorithm simulates the characteristic behavior of the classical modes of electrophoresis, which is shown by examples involving moving boundary electrophoresis and isoelectric focusing. In the first example two different integration schemes are used and their accuracy and stability investigated. The second example illustrates the versatility of the methodology.

O. A. PALUSINSKI, A. GRAHAM,
R. A. MOSHER, and M. BIER

Biophysics Technology Laboratory and
Department of Electrical and
Computer Engineering
University of Arizona
Tucson, AZ 85721

D. A. SAVILLE

Department of Chemical Engineering
Princeton University
Princeton, NJ 08544

SCOPE

In the model presented in Part I (Saville and Palusinski), the electrophoresis of amphoteric compounds is described by a set of partial differential equations coupled to a system of algebraic equations. Separation of sample components arises from interactions between the chemical equilibria and the transport processes. These interactions alter the effective mobilities of the various species and induce them to separate under the action of the electric field in nonequilibrium processes such as isotachophoresis. In equilibrium processes such as isoelectric focusing, the action of the field produces a pH gradient and the amphoteric constituents move to positions where they are isoelectric. In either case, the evolution of the process is best followed by numerical methods.

The purpose of this paper is twofold:

1. To show how the mathematical model derived in Part I can be expressed in a form suitable for numerical computation.

2. To demonstrate the model depicts the detailed characteristics of electrophoretic processes.

The numerical algorithm selected employs a five-point finite-difference expression to approximate the spatial derivatives at a set of mesh points. This converts the set of partial differential equations into a set of ordinary differential equations describing the temporal evolution of the concentration fields at each mesh point. These equations can be integrated using any one of a variety of schemes for solving sets of first-order ordinary differential equations. Boundary conditions at either end of a separation column are incorporated by adjusting the form of the finite-difference expressions at the boundary points. In a similar fashion, the algorithm can easily be adapted for simulation of novel separation methods such as the use of immobilized ampholytes, molecular sieving, or ion-selective membranes at the boundaries.

CONCLUSIONS AND SIGNIFICANCE

The implementation of the algorithm describing electrophoretic transport processes is illustrated by simulating moving boundary electrophoresis and isoelectric focusing with immobilized species. Both examples are intended to illustrate particular electrophoretic processes using rather simple systems. Attention concentrates on the essential characteristics of a particular mode. For the isoelectric focusing example, the central feature is the migration of the sample to its isoelectric point; for moving boundary electrophoresis, it is the Kohlrausch adjustment of the self-sharpening front. The model depicts these features correctly and in detail.

We have demonstrated that the model derived in Part I, translated into a finite difference form suitable for implementation on a digital computer, can be used to simulate certain electrophoretic separations. The resulting numerical scheme exhibits the features sought in complicated problems of this

sort, namely, a stable solution that evolves smoothly when suitable small step sizes are used, and a loosely defined convergence as the step sizes are made smaller. The major computational problem concerns the need to use small spatial step sizes at high current levels.

The computational model has already proved useful in studies of various electrophoretic separation processes; recent experimental work has served to validate quantitative and qualitative features of the model (Mosher et al., 1985). In that study, zone structure in isotachophoresis was monitored using a conductivity detector, and what were thought to be anomalous peaks were found. Numerical calculations using the model presented here with buffer characteristics corresponding to the experiment showed that the peaks were, in fact, intrinsic features of the buffer system.

INTRODUCTION: THE CLASSICAL MODES OF ELECTROPHORESIS

In Part I of this paper (Saville and Palusinski), a model of electrophoretic processes was presented. Such a model is suitable for the description of analytical electrophoretic systems, which vary in terms of the initial distribution of solute components along the axis of a separation column and the boundary conditions (i.e., the permeability to individual constituents) at the ends of the column. There are myriads of combinations and permutations of these two factors, but certain idealized situations have been singularly effective in practice. These are known as zone electrophoresis (ZE), moving boundary electrophoresis (MBE), isotachophoresis (ITP), and isoelectric focusing (IEF). They can be considered collectively as the classical model of electrophoresis, being based on constraints first studied by Hittorf (1853) and Kohlrausch (1897).

Kohlrausch demonstrated that an electric current can give rise to changes in concentration within an electrolyte system only where the system is nonhomogeneous. Three distinct types of inhomogeneities were considered. At the unavoidable interface between an electrode and a solution, electrochemical reactions produce new species and induce concentration changes, as first studied by Hittorf. These changes are utilized in IEF, while they are suppressed in MBE, ZE, and ITP through the use of large electrode buffer volumes. The essential feature of IEF is that separations are carried out within pH gradients. These gradients start to form at the electrodes and propagate inward. Thus, only in IEF can one start with a uniform distribution of all components throughout the column. The end result will be a stationary steady state with all amphoteric constituents arranged according to their isoelectric points.

A second type of inhomogeneity results from a simple dilution of the electrolytes. Such concentration profiles do not migrate electrophoretically but broaden due to diffusion. In practice these are encountered as the stationary boundaries in MBE (Tiselius, 1937), or in ITP at the site of the so-called terminator concentration adjustments.

The third type of inhomogeneity considered by Kohlrausch arises at a boundary across which one or more species disappear. These boundaries migrate in an electric field, but different patterns are encountered in ITP, ZE, and MBE.

ITP is typically carried out in discontinuous buffer systems where the sample is inserted at the interface between the leading and terminating electrolytes. If the net mobilities of all sample constituents are bracketed by the net mobilities of leading and terminating electrolytes, the application of an electric field will result in the establishment of a migrating steady state. All the sample constituents will sort themselves in contiguous zones in order of decreasing mobilities (Everaerts et al., 1976; Bier and Allgyer, 1979). The self-sharpening boundaries all migrate with the same velocity, and within each zone physical properties such as concentration, temperature, refractive index, electric field, and pH are uniform. It is of some significance that this migrating steady state of ITP, as well as the stationary steady state of IEF, have no counterparts in any chromatographic or field flow fractionation technique; they are unique to electrophoresis.

In contrast, ZE and MBE are typically conducted in a uniform background of buffer electrolyte throughout the column and electrode reservoirs. Sample constituents migrate at their own characteristic velocity. In MBE the sample zone is sufficiently long to permit separate observation of leading and trailing boundaries. Depending on the effective mobilities of sample and buffer constituent ions, one of the boundaries will be self-sharpening, as in ITP, while the other boundary will broaden due to the combined effect of diffusion and migration. The sample zone is much shorter in ZE, thus there is strong interaction between the advancing and trailing boundaries. Constant boundary shapes are impossible, and the constituent sample zones are asymmetric. Because of their broadening, the peak concentration within each zone continually decreases.

These characteristics of the four modes have been reproduced by the model (Bier et al., 1983), but in the modeling of other electrophoretic techniques, additional constraints not considered by Kohlrausch or Hittorf may be necessary. For instance, pore density gradient electrophoresis, widely used for molecular weight estimation, can be modeled by decreasing the mobility of constituents along the axis of the separation column. Co- or counterflow of buffer can also be incorporated in the model. The same holds true for the imposition of specific ion permeabilities at the column ends, irrespective of how such selective permeability is actually achieved, e.g., by selection of an appropriate membrane. Additionally, preparative electrophoretic techniques may require some sort of forced convention for the recovery of separated fractions, as in continuous flow electrophoresis (Saville, 1980) or recycling isoelectric focusing.

Here we shall consider application of the model to describe analytical electrophoretic techniques where the experiments are carried out in systems that can be considered as one-dimensional, e.g., columns where flow is absent. The one-dimensional model has been implemented on a digital computer and will be described together with selected applications.

REFORMULATION OF THE MATHEMATICAL MODEL

As outlined in Part I, the mathematical model consists of a set of coupled equations, algebraic relations describing chemical equilibria involving water and other ionogenic species and partial differential equations arising from the appropriate balance laws. For simplicity, we will consider the case of I biprotic ampholytes along with the dissociation products of water. Henceforth the equations are scaled and stated in one (Cartesian) dimension with flow absent.

Equilibrium Expressions for the Ampholytes and Water ($2I+1$ equations)

$$K_i^{(-)} = n_1 n_{3i+2}/n_{3i} \tag{1}$$

$$K_i^{(+)} = n_1 n_{3i}/n_{3i+1} \tag{2}$$

$$K_w \stackrel{d}{=} K_0 n_0 = n_1 n_2 \tag{3}$$

Ampholyte Balances (I equations)

$$\frac{\partial}{\partial t}(n_{3i} + n_{3i+1} + n_{3i+2}) = -\frac{\partial}{\partial x}(f_{3i} + f_{3i+1} + f_{3i+2}) \tag{4}$$

$$f_i \stackrel{d}{=} -z_i \Omega_i n_i \frac{\partial \phi}{\partial x} - \Omega_i \frac{\partial n_i}{\partial x} \tag{5}$$

Current Balance (one equation)

$$0 = \frac{\partial}{\partial x} \sum_{k=1}^{N} z_k f_k \tag{6}$$

The Local Electrical Neutrality Condition (one equation)

$$\sum_{k=1}^{N} z_k n_k = 0 \tag{7}$$

There are $3I+3$ equations to account for the $3I+3$ dependent variables: $3I$ from the ampholytes, two from water, and one from the potential gradient.

In its present form the model is unsuited for numerical work so further transformations are in order. The discussion will be simplified using matrix notation and we therefore introduce:

A vector of neutral species concentrations

$$u^T = (n_3, n_6, \ldots n_{3I}) \tag{8}$$

A vector of charged species concentrations

$$v^T = (n_1, n_2, n_4, n_5, \ldots, n_{3I+1}, n_{3I+2}) \tag{9}$$

A vector of total component concentrations

$$y^T = (y_1, y_2, \ldots, y_I) \tag{10}$$

where

$$y_i = n_{3i} + n_{3i+1} + n_{3i+2}; \quad i = 1, \ldots, I \tag{11}$$

A vector of mobilities

$$S^T = (\Omega_1, -\Omega_2, \Omega_4, -\Omega_5, \ldots, \Omega_{3I+1}, -\Omega_{3I+2}) \tag{12}$$

A vector of charged species concentrations and mobilities determining the electric transport

$$p^T = (p_1, \ldots, p_I) \tag{13}$$

where

$$p_i = \Omega_{3i+1} n_{3i+1} - \Omega_{3i+2} n_{3i+2}; \quad i = 1, \ldots, I \tag{14}$$

We shall also use the following matrices:

$$R = [r_{ij}]; \quad i = 1, \ldots, I \qquad j = 1, \ldots, 2(I+2) \tag{15}$$

where

$$r_{ij} = \begin{cases} \Omega_{3i+1}; & j = 2i+1 \\ \Omega_{3i+2}; & j = 2i+2 \\ 0 \quad ; & k \neq 2i+1 \text{ and } j \neq 2i+2 \end{cases}$$

$$Q = [q_{ij}]; \quad i,j, = 1, \ldots, I \tag{16}$$

where

$$q_{ij} = \begin{cases} \Omega_{3i}; & i = j \\ 0 \quad ; & \text{otherwise} \end{cases}$$

It will be convenient to utilize a scalar function notation for the dimensionless conductivity

$$\sigma(v) \stackrel{d}{=} \sum_{k=1}^{N} z_k^2 \Omega_k n_k \tag{17}$$

Furthermore, the current balance, Eq. 6, may be integrated to give

$$\sum_{k=1}^{N} z_k f_k = \eta \tag{18}$$

where the integration constant, $\eta = \eta(t)$, represents the dimensionless current density.

Substituting the expressions for the fluxes, Eq. 5, in Eq. 18 and making use of notation given in Eq. 17, gives an equation for the electric field as

$$\frac{\partial \phi}{\partial x} = \eta + S^T \frac{\partial v}{\partial x} \sigma(v)^{-1} \tag{19}$$

The local electroneutrality equation is reformulated by noting that Eqs. 1–3 and Eq. 11, when rearranged, give:

$$n_{3i} = y_i \left[1 + \frac{n_1}{K_i^{(+)}} + \frac{K_i^{(-)}}{n_1} \right]^{-1} \quad i = 1, \ldots, I \tag{20}$$

Equation 7 becomes

$$n_1 - \frac{K_w}{n_1} + \sum_{i=1}^{I} \left[\frac{n_1}{K_i^{(+)}} - \frac{K_i^{(-)}}{n_1} \right] n_{3i} = 0 \tag{21}$$

This nonlinear equation for n_1 given y is written symbolically as

$$L^*(n_1; y) = 0 \tag{22}$$

Finally, using the definitions embodied in Eqs. 8–17 along with Eq. 19 allows one to express Eq. 4 in the form

$$\frac{\partial y}{\partial t} = \frac{\partial}{\partial x}\left[p(v) \frac{\partial \phi}{\partial x} + Q \frac{\partial u}{\partial x} + R \frac{\partial v}{\partial x} \right] \tag{23}$$

The transformed model consists of (partial differential) Eqs. 23, 22, 20, and 1–3 defining the concentrations of neutral and charged species. The electric field is defined by Eq. 19.

Numerical Treatment

The partial differential equations and the algebraic relations are nonlinear and iterative; numerical methods must be used to solve them. Our approach utilizes a technique whereby the spatial derivatives are replaced by finite difference approximations which yields a set of ordinary differential equations with time as the independent variable. The principal advantage of this approach, sometimes called the method of lines (Ames, 1977), is that sophisticated algorithms and computer codes are available for solving large systems of ordinary differential equations efficiently with variable step sizes and control over error growth.

Accordingly, the region of interest, $0 < x < x_{max}$, is overlaid with a set of M grid points where $\Delta x = x_{max}/(M-1)$. The index j denotes the grid point in question using the notation $x_1, \ldots, x_j, \ldots, x_M$. Values of the dependent variables at the point in question are also delineated using subscripts, e.g.,

$$u(x_j, t) = u_j(t) = u_j \tag{24}$$

The finite-difference approximation for the spatial derivatives is based on the central difference approximation

$$\left.\frac{\partial u}{\partial x}\right|_{x=x_j} = \frac{u_{j+1} - u_{j-1}}{2\Delta x} \tag{25}$$

and we write

$$\left.\frac{\partial u}{\partial t}\right|_{x=x_j} = \frac{d}{dt} u_j \tag{26}$$

Using the notation

$$F \stackrel{d}{=} p(v)\frac{\partial \phi}{\partial x} + Q\frac{\partial u}{\partial x} + R\frac{\partial v}{\partial x} \tag{27}$$

we write the partial differential equation 23, in the form

$$\frac{\partial y}{\partial t} = \frac{\partial F}{\partial x} \tag{28}$$

Using the differencing in Eq. 25, we obtain

$$\frac{dy_j}{dt} = \frac{1}{2\Delta x}[F_{j+1} - F_{j-1}]; \quad j = 2, \ldots, M-1 \tag{29}$$

where

$$F_j = p(v_j)\left.\frac{\partial \phi}{\partial x}\right|_j + \frac{1}{2\Delta x}[Q(u_{j+1} - u_{j-1}) + R(v_{j+1} - v_{j-1})] \tag{30}$$

with

$$\left.\frac{\partial \phi}{\partial x}\right|_j = \left(\eta + S^T\frac{v_{j+1} - v_{j-1}}{2\Delta x}\right)\sigma^{-1}(v_k)$$

For points near the boundaries, i.e., $j = 1$ or M, the formulas are modified by using forward or backward, instead of central, differences.

The boundary conditions for processes such as ZE, MBE, and ITP are straightforward: the rate of change of concentration is zero. The principal difficulty encountered arises from the fact that these conditions are obtained asymptotically as $x \to \pm\infty$ but must be enforced at finite distances in any numerical scheme. In some of our work this has necessitated use of an "observational window" that defines a movable grid. The computational algorithm advances this window at the migration rate of the fastest moving species and this enables us to avoid excessive computer time and storage requirements. In processes such as IEF the ends of the column are fixed and there is no need to employ a moving grid. Moreover in IEF the boundary conditions are expressed in terms of the permeability to various ions.

The set of ordinary differential equations can be integrated numerically using one of several known schemes. For example, the Runge-Kutta-Merson and the Fehlberg schemes have been used with improved automatic step size control (Watts, 1984), as have two fixed step size schemes known as the Euler method and modified Euler (Heun's) method (Lapidus and Seinfeld, 1971; Carnahan et al., 1969). The results described here were obtained with the schemes implemented in a specialized software package based on the DAREP simulation language (Korn and Wait, 1978).

Adjoined to this system of ordinary differential equations is a local (nonlinear) equation, Eq. 21, which must be solved at each grid point x_j. This equation is normally solved using a Newton iteration scheme that usually converges quickly due to the availability of good initial values from previous time steps. Solutions for the initial condition are obtained by an algorithm based on inverse interpolation and bisection; this procedure is also used if the Newton iteration scheme does not converge.

NUMERICAL SIMULATION OF ELECTROPHORETIC PROCESSES

One of the purposes of this paper is to provide detailed descriptions of results obtained with our computational algorithm for two representative situations: moving boundary electrophoresis and isoelectric focusing. The moving boundary problem was selected to illustrate the model's ability to depict the Kohlrausch adjustments in concentration and the motion of a self-sharpening front. Because there is only one sample constituent present, no "separation" is involved and the effects of changes in step size can be explored relatively economically. On the other hand, the presence of weak electrolytes and an ampholyte renders the simulated system far too complex for the simple application of one of the Kohlrausch regulating functions, and computer solution is essential. In the second example a compound is focused to its isoelectric point to illustrate the ability of the model to track the migration of a substance to a steady state distribution that is maintained by a balance between diffusion and electromigration. All program output has been rescaled to provide dimensional data.

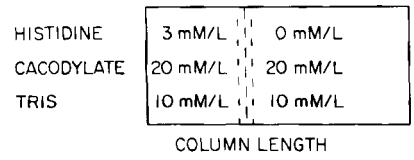

Figure 1. Initial distribution of components in a simulation of moving boundary electrophoresis; anode is to the right. Component properties characterized by values of pK and mobility μ, ($m^2/V \cdot s$): cacodylate – $pK = 6.21$, $\mu = 2.31 \cdot 10^{-8}$; TRIS – $pK = 8.3$, $\mu = 2.41 \cdot 10^{-8}$; histidine – $pK_1 = 6.04$, $pK_2 = 9.17$, $\mu = 2.02 \cdot 10^{-8}$.

Moving Boundary Electrophoresis

In practice, large electrolyte reservoirs are used to negate the influence of reactions occurring at the electrodes. This makes the concentrations at the column ends constant and effectively renders the system infinitely long.

In the simulation two weak electrolytes, cacodylic acid (cacodylate) and tris (hydroxymethyl)-aminomethane (TRIS) play the role of buffer, uniformly distributed throughout the column. The sample, histidine, an amino acid, occupies only part of the column. This is shown schematically in Figure 1.

The initial, sharp histidine boundary is depicted as the zero time profile in Figure 2a. This was the product of 1 min of diffusion to smooth the boundary, as sharper profiles tend to cause numerical oscillations when current is applied. The time progression in this figure is from left to right, the profiles depict the histidine concentration after passage of a current of 36.0 A/m^2 for 3, 6, and 9 min. The simulation demonstrates that a steady-state, self-sharpening front is developed. The sharp node resides at the position of the initial histidine profile and reflects the establishment of a stationary diffusing boundary. The behavior of the histidine concentration is typical of the Kohlrausch readjustment in ITP, which can be considered as a special case of MBE. A numerical example of the application of the Kohlrausch regulating function is given in the Appendix. Note that this system meets the mobility requirements for a stable boundary: the effective mobility of histidine, the trailing species, is lower than that of TRIS, the leader. This is due to the lower degree of dissociation of histidine in this pH range.

Figures 2b and 2c display the corresponding behavior for TRIS and cacodylate, respectively. Each of these components also exhibits a stationary, diffusing boundary and a migrating, self-sharpening boundary. The movement of histidine into this region of the column causes an evacuation of the background buffers, behavior that is also explained by the Kohlrausch regulating function. Figures 3a and 3b present the conductivity and pH data that correspond to these concentration profiles.

Due to the complicated nonlinear structure of the model it is relatively fruitless to attempt to study characteristics of the numerical method by analytical techniques. Matters of stability and convergence must be examined by numerical simulation experiments. Accordingly we have used the two fixed-time step

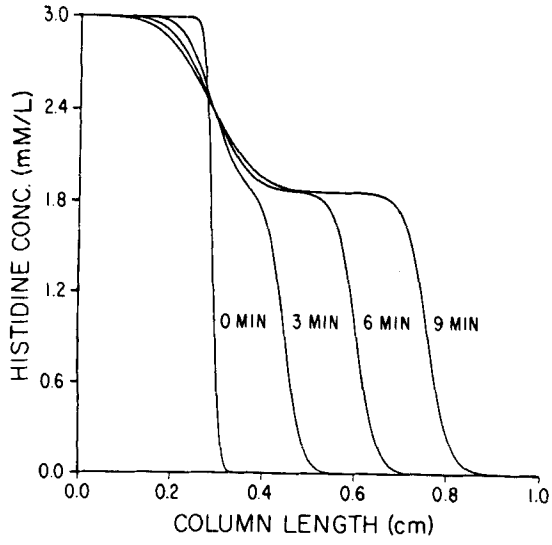

(a) Motion of the histidine boundary.

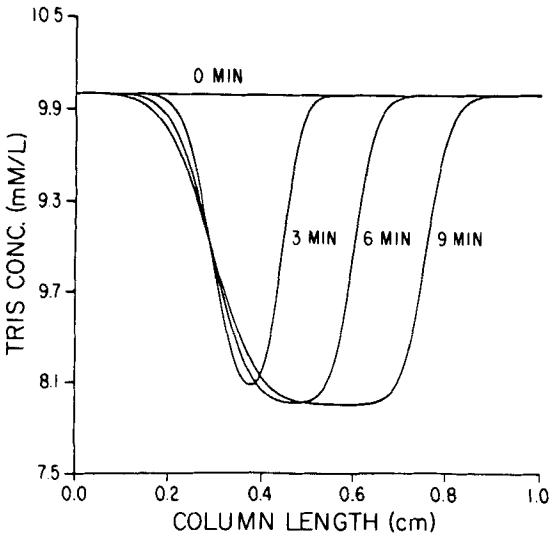

(b) Motion of the TRIS boundary.

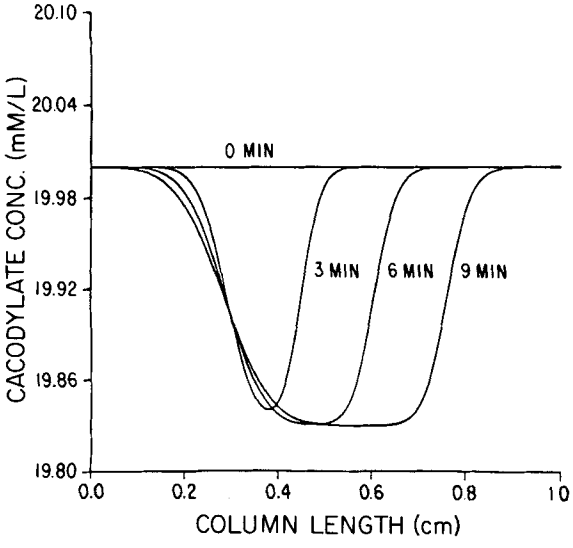

(c) Motion of the cacodylate boundary.

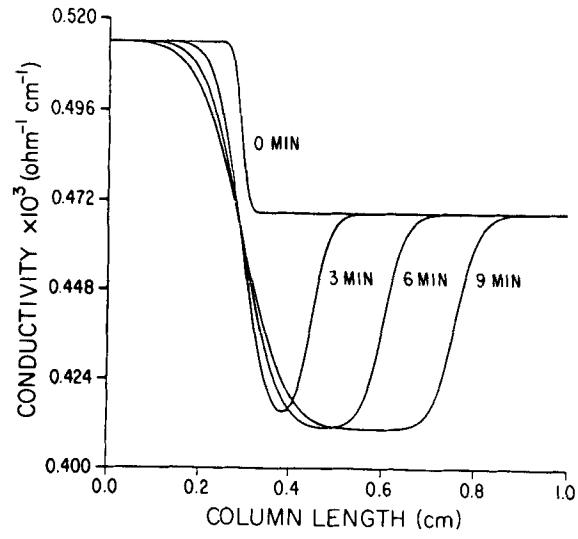

(a) Conductivity profiles.

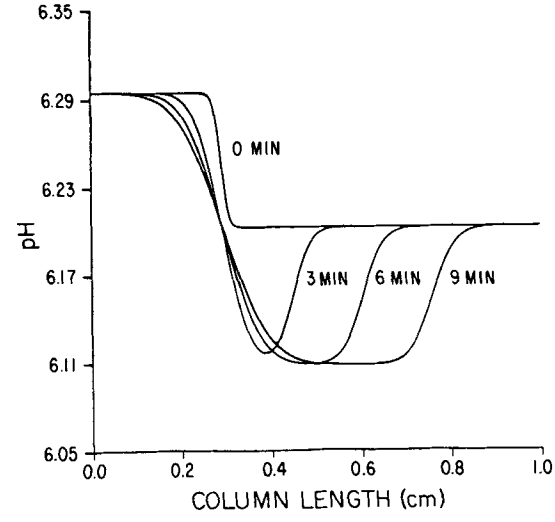

(b) pH profiles.

Figure 3. Simulation of moving boundary electrophoresis.

schemes mentioned earlier to test these features of the algorithm. Although it is not always easy to judge beforehand whether a particular mesh size and time step will be suitable in a new situation, the computation scheme renders judgment quickly in the form of undamped oscillations. Given a set of constituents and a particular mode of electrophoresis (specified by the initial distribution of constituents, boundary conditions, and current) the selection of mesh size and time step depends heavily on experience acquired in previous simulations. Once a stable set of step sizes has been found, as judged by smooth evolution of the concentration fields, the mesh can be refined

Figure 2. Simulation of moving boundary electrophoresis at a current density of 36.9 A/m²; computation with Heun integration algorithm with 401 mesh points in the 1 cm column and a time step of 0.02 min. The Kohlrausch readjustment of the concentration of the advancing steady state boundary is clearly visible; it creates a dilution boundary at the location of the initial histidine boundary.

Table 1. Effects of Grid Size and Time Step Size on Histidine Concentrations at 30% of Column Length; Euler Integration

	Number of Mesh Points					
	51		101		201	
$\Delta\hat{x}$, cm(*)	2×10^{-2}		1×10^{-2}		5×10^{-3}	
$\Delta\hat{t}$, min	0.025	0.05(‡)	0.1	0.2(‡)	0.05	0.1(‡)
$a\Delta\hat{t}/(\Delta\hat{x})^2$(**)	9.68×10^{-2}	1.025×10^{-1}	1.54	3.08	3.08	6.16
Time, min						
0	1.500	1.500	1.500	1.500	1.500	1.500
1	2.494	2.509	2.377	2.345	2.363	2.371
2	2.371	2.361	2.410	2.374	2.407	2.406
3	2.421	2.426	2.408	2.426	2.407	2.399
4	2.404	2.402	2.406	2.614	2.406	2.374
5	2.406	2.407	2.405	3.091	2.405	2.306
6	2.405	2.405	2.404	3.814	2.404	2.325
7	2.404	2.404	2.404	−1.854E2	2.404	4.706E3
8	2.404	2.404	2.403	−9.732E3	2.403	−5.432E6
9	2.404	2.404	2.403	−4.902E3	2.403	−1.265E9

* All computations are carried out in dimensionless form and converted to dimensional form to facilitate interpretation. Histidine concentrations are expressed in mmol/L.
** The symbol a denotes the scale factor needed to render the ratio dimensionless.
† This solution appears marginally unstable.
‡ These solutions appear unstable.

to satisfy the required accuracy at the minimum of computational effort.

We have investigated the effects of step size (both spatial and temporal) in several modes. Some results obtained in connection with the moving boundary mode are reported here. The numerical experiments on stability and convergence were done with four different mesh sizes, Δx, and several time-step sizes, Δt, with the Euler and Heun (improved Euler) integration schemes (Carnahan et al., 1969) to find the maximum Δt at which the solution is stable. The results are summarized in Tables 1 and 2 and Figures 4 and 5. Values of the dimensionless quantity $a\Delta\hat{t}/(\Delta\hat{x})^2$ are also shown in the tables, (the symbol a represents the scale factor). It will be recalled that numerical solutions of the parabolic diffusion equation using an explicit method with a three-point formula for the spatial derivative require $a\Delta\hat{t}/(\Delta\hat{x})^2 < \frac{1}{2}$ for stability (Richtmyer and Morton, 1967; Carnahan et al., 1969). Using a five-point finite-difference formula for the spatial operator (as was used in the calculations under discussion) produces more stringent limits, viz., $a\Delta\hat{t}/(\Delta\hat{x})^2 < \frac{3}{16}$ for the simple diffusion equation. Thus, it should be obvious from the tables that such simple criteria are inadequate indicators of stability here. This is clearly shown by the results provided using the Euler method with two different combinations of mesh and time step sizes but the same value of the dimensionless quantity $a\Delta\hat{t}/(\Delta\hat{x})^2$, namely, 3.08 (Table 1).

Using the Heun scheme for the temporal integration allows substantially larger time step sizes to be employed. Tables 1 and 2 show that with a given mesh size, a time step as much as five times as large can still yield a stable scheme (0.25/0.05 for the Heun method as compared to the Euler scheme for $\Delta\hat{x} = 0.02$). Inspection of these tables also discloses that the second-order method yields more accurate results. If we take the results from the 401 mesh point Heun computation as the benchmark solution, then at any grid spacing the Heun computation is more accurate than the Euler scheme even though the time steps are larger. Table 3 shows the relative amounts of computer time required for the different methods.

Figure 4 compares the histidine profile computed by the 401

Table 2. Effects of Grid Size and Time-Step Size on Histidine Concentrations at 30% of Column Length; Heun Integration

	Number of Mesh Points							
	51		101		201		401	
$\Delta\hat{x}$, cm	2×10^{-2}		1×10^{-2}		5×10^{-3}		2.5×10^{-3}	
$\Delta\hat{t}$, min	0.25	0.50(‡)	0.25	0.50(‡)	0.10	0.25(‡)	0.02	0.05(‡)
$a\Delta\hat{t}/(\Delta\hat{x})^2$	0.968	1.935	3.87	7.74	6.19	15.48	4.95	12.38
Time, min								
0	1.500	1.500	1.500	1.500	1.500	1.500	1.500	1.500
1	2.447	2.353	2.342	2.669	2.351	2.016	—	—
2	2.384	2.423	2.403	5.252	2.405	−1.283E4	—	—
3	2.413	2.345	2.407	−2.303E2	2.407	−5.188E6	2.407	3.914E15
4	2.406	2.436	2.406	−5.715E2	2.406	−5.638E8	—	—
5	2.406	2.418	2.405	3.189E3	2.405	−2.989E10	—	—
6	2.405	2.369	2.404	−3.189E3	2.404	−1.926E12	2.404	−1.383E29
7	2.404	2.423	2.404	1.225E4	2.404	−1.154E14	—	—
8	2.404	2.419	2.403	7.761E3	2.403	−9.569E15	—	—
9	2.404	2.371	2.403	3.939E4	2.403	−1.625E18	2.403	−6.753E41

† This solution appears marginally unstable.
‡ These solutions appear unstable.

Table 3. Computer* CPU Time(s) in MBE Simulations

Mesh Size	Method	
	Heun	Euler
51	7.4	12.3
101	22.5	23.0
201	84.5	83.8
401	239.6	N.A.

* Cyber 175

mesh point Heun method with the 51 mesh point Euler scheme. In the moving boundary mode, unstable numerical behavior often manifests itself at the transition to the Kohlrausch step, as noted here for the 51-point scheme. Figure 5 shows the convergence of the Heun scheme as the number of spatial grid points is increased. The Euler computations also converged to the 401 grid point Heun solution as grid spacing decreased. It is clear that the greatest discrepancies occur in those parts of the electrophoresis column where concentrations are rapidly changing. Nevertheless, when a scheme is stable it is possible to follow the movement of a front using a moving grid scheme over extended time periods (Bier et al., 1983).

Isoelectric Focusing

A significant recent advance in experimental IEF is the use of tailor-made, immobilized pH gradients formed by copolymerization of ionizable groups into the usual polyacrylamide gel matrix. The versatility of the computation scheme can be illustrated by modeling this separation technique in a one-dimensional gel column. The immobilized pH gradient was simulated by assigning a value of zero to the mobility coefficient of the ionic constituents of the gradient, cacodylic acid and TRIS. As the initial condition, histidine was uniformly distributed throughout the column, Figure 6. In addition, conditions were imposed to render the boundaries impermeable to all except hydrogen and hydroxyl ions. This simulates experimental conditions where minimal electrode buffer volumes are utilized and the current to the electrodes is carried by hydrogen and hydroxyl ions alone.

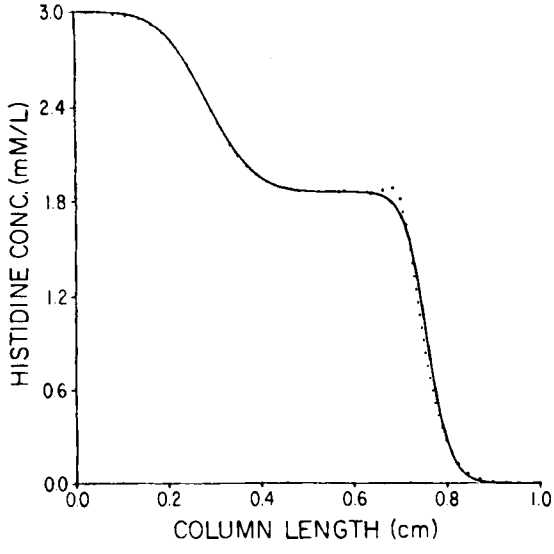

Figure 4. Comparison of two integration schemes. ____ histidine profile corresponding to 9 min of migration according to Heun integration data presented in Figure 2a. ..... profile obtained by Euler integration algorithm, with 51 mesh points in the 1 cm column and a time step of 0.025 min.

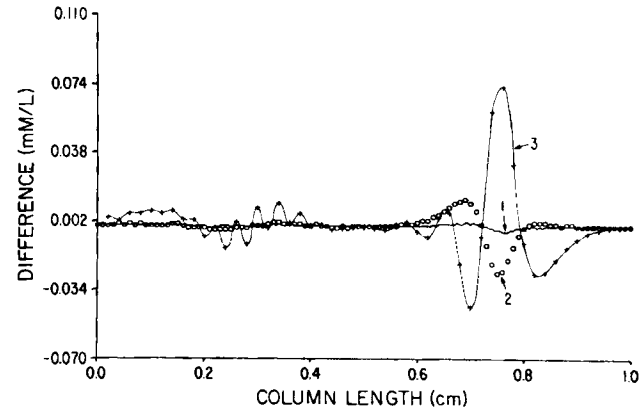

Figure 5. Convergence of Heun integration scheme showing differences between the 9 min histidine profiles at corresponding column positions.
Line 1: Heun results (401-201 mesh points.
Line 2: Heun results (401-101 mesh points).
Line 3: Heun results (401-51 mesh points).

The evolution of the histidine concentration profiles at a constant current density of 0.2 A/m² is presented in Figure 7a. As expected, histidine concentrates in the column region closest to its isoelectric point, leaving other parts of the column virtually histidine-free. This has direct consequences on the conductivity profiles, shown in Figure 7b. In the histidine-free parts of the column, the conductivity is very low, and current is carried by hydrogen and hydroxyl ions. Figure 8 shows the final histidine profiles at the three current densities of 0.1, 0.2, and 0.4 A/m². As expected, processes with higher current densities result in sharper focusing.

The computations of these profiles were carried out using 51 grid points to cover the column and a variable time step size Runge-Kutta scheme to integrate the ordinary differential equations. The corrugation apparent in some of the profiles is traced to regions of low conductivity; the use of a finer spatial grid supresses the corrugations.

CONCLUSION

In work done thus far, effort has centered on testing the ability of the algorithm to handle a variety of electrophoretic modes: zone electrophoresis, moving boundary electrophoresis, isotachophoresis, isoelectric focusing, and electrodialysis (Bier et al., 1983), and no more than five components have

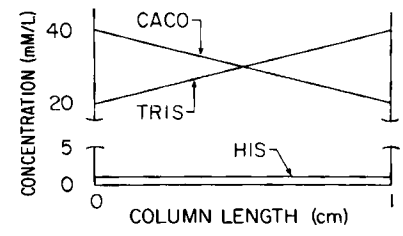

Figure 6. Initial distribution of components in the isoelectric focusing simulation. A mobility of zero was assigned to the two buffer constituents, cacodylate and TRIS; the mobility of histidine was 2.02 · 10^{-8} ($m^2/V \cdot s$).

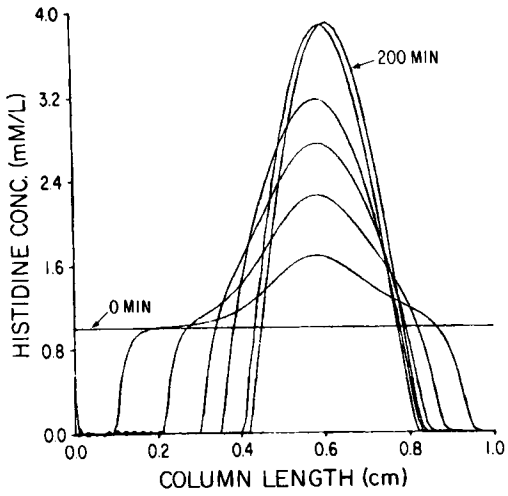

(a) Histidine concentration profiles for 0, 10, 20, 30, 40, 80, and 200 min of focusing.

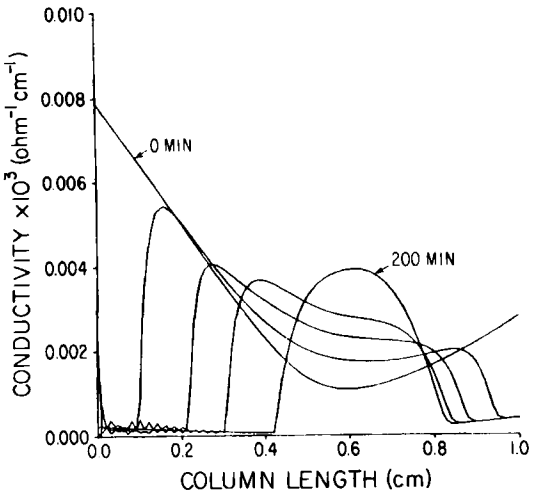

(b) Conductivity profiles corresponding to 0, 10, 20, 30, and 200 min of focusing. Conductivity is dominated by the concentration of histidine at the pH imposed by the immobilized gradient.

Figure 7. Simulation of isoelectric focusing in an immobilized gradient of cacodylate and TRIS at constant current density of 0.2 A/m²; integration by the Runge-Kutta variable time step algorithm with 101 mesh points.

been used. Further expansion is simply a matter of more computer storage space and more processing time or faster processors. Indeed, the inclusion of noninteracting samples such as proteins in trace quantities is quite straightforward. However, the handling of proteins in other than trace quantities will require a more sophisticated treatment, since protein dissociation is complex. Assignment of individual dissociation constants to each ionizable group appears impractical and a simplified model of their dissociation or actual experimental data in the form of a computer tables will have to be used. Expansion of the model to two or three dimensions will provide an important tool to study a wider variety of electrophoretic phenomena, e.g., the effects of electroosmosis on separation processes. However such expansion will require further specialized software development.

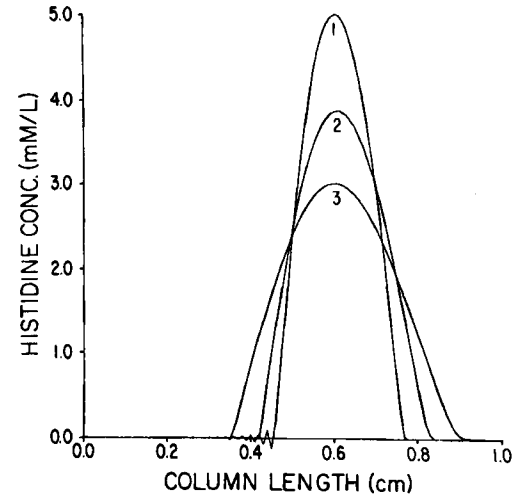

Figure 8. Effect of current density on steady state histidine profiles resulting from focusing in the immobilized gradient of Figure 6. Current densities corresponding to profiles 1, 2, and 3 were 0.4, 0.2, and 0.1 A/m², respectively.

ACKNOWLEDGMENT

This research was supported in part by the NSF Grants CPE 8103079 and CPE 8311125 from the Division of Chemical and Process Engineering (Separation Process Program), and in part by NASA Contract NAS8-32950 and NASA Grant NSG-7333 administered by the Microgravity Science and Applications Program.

NOTATION

Dimensionless Constants and Variables

f_i = flux of the ith species
F = vector of total fluxes
I = total number of biprotic ampholytes
K_0 = equilibrium constant for water
$K_i^{(-)}$ = constant describing the equilibrium between the neutral and negatively charged species of the ith ampholyte
$K_i^{(+)}$ = constant describing the equilibrium between the neutral and the positively charged species of the ith ampholyte
K_w = dissociation constant for water
n_0 = water concentration
n_1 = hydrogen ion concentration
n_2 = hydroxyl ion cocentration
n_i = concentration of the ith species
M = number of mesh points
N = total number of ionic species
P = vector of charged species concentrations weighed by their mobilities
Q = matrix of mobility coefficients of neutral species (derived from their diffusivities)
R = matrix of mobility coefficients of charged species
S = vector of mobilities
t = time
u = vector of neutral species concentrations
v = vector of charged species concentrations
x = position
x_{max} = maximum value of the dimensionless spatial variable
y = vector of component (total) concentrations
z_i = valence of the ith species

Dimensional Variables

$\hat{x}$ = position, m
$\hat{t}$ = time, s

Greek Letters

Δ = denotes a difference taken across a boundary
η = current density
σ = dimensionless conductivity
ϕ = electric potential
Ω_i = mobility coefficient of the ith species
Δt = integration time step
Δx = distance between mesh points

APPENDIX: KOHLRAUSCH REGULATING FUNCTION EXAMPLE

To show that the changes noted in Figures 2 and 3 for the concentrations across the step are consistent with the Kohlrausch adjustment we use numerical data from a stable simulation with 51 grid points. The conditions on either side of the self-adjusting front are

	Behind	Ahead
Cacodylate	19.83 mM/L	20.00 mM/L
TRIS	7.951 mM/L	10.00 mM/L
Histidine	1.867 mM/L	0.00 mM/L
pH	6.108	6.203
Conductivity	4.104×10^{-4} $\text{ohm}^{-1} \cdot \text{cm}^{-1}$	4.685×10^{-4} $\text{ohm}^{-1} \cdot \text{cm}^{-1}$

The pK values are provided in the legend of Figure 1. The degree of ionization for each component is

	Behind	Ahead
Cacodylate	0.4416	0.4960
TRIS	0.9936	0.9921
Histidine	0.4609	—

From Part I, Eqs. 21 and 22, we obtain

$$\frac{v}{\eta} = \frac{\Delta[\Omega_{3i+1} n_{3i+1} - \Omega_{3i+2} n_{3i+2}]/\sigma}{\Delta[n_{3i} + n_{3i+1} + n_{3i+2}]}$$

in terms of the jumps across the front.

From the data given, the ratio v/η calculated for cacodylate, TRIS, and histidine is 0.222, 0.227, and 0.227, respectively, showing that the conditions on either side of the step are consistent with the stipulations of a Kohlrausch adjustment.

LITERATURE CITED

Ames, W., *Numerical Methods for Partial Differential Equations*, Academic Press, New York, Ch. 2, 5 (1977).

Bier, M., and T. Allgyer, "Isotachophoresis," in *Electrokinetic Separation Methods*, P. G. Righetti, C. J. van Oss, and J. W. Vanderhoff, eds., Elsevier North Holland, 443 (1979).

Bier, M., et al., "Electrophoresis Mathematical Modeling and Computer Simulation," *Science*, **219**, 1,281 (1983).

Carnahan, B., H. A. Luther, and J. O. Wilkes, *Applied Numerical Methods*, Wiley, New York, Ch. 7 (1969).

Everaerts, F. M., J. L. Beckers, and Th. P. E. M. Verheggen, *Isotachophoresis: Theory, Instrumentation and Applications*, Elsevier Scientific, Amsterdam (1976).

Hittorf, J. W., "Ueber die Wanderungen der Ionen wahrend der elektrolyse," (On Ion Transport During Electrolysis), *Poggendorff's Ann.*, 89, 177 (1853).

Kohlrausch, F., "Ueber Concentrations-Verschiebungen durch Elektrolyse im Innern von Losungen und Losungsgemischen" (On Concentration Displacements Inside Solutions and Solution Mixtures by Means of Electrolysis), *Ann. Phys.* (Leipzig), 62, 209 (1897).

Korn, G. A., and J. V. Wait, *Digital Continuous System Simulation*, Prentice Hall, Englewood Cliffs, NJ, Ch. 4 (1978).

Lapidus, L., and J. H. Seinfeld, *Numerical Solution of Ordinary Differential Equations*, Academic Press, New York, 118 (1971).

Mosher, R. A., W. Thormann, and M. Bier, "Computer-Aided Analysis of Electric Field Gradients within Isotachophoretic Boundaries between Weak Electrolytes," *J. Chromatogr.*, 320, 23 (1985).

Richtmyer, R. D., and K. W. Morton, *Difference Methods for Initial-Value Problems*, Wiley, New York, Ch. 4 (1967).

Saville, D. A., "The Fluid Mechanics of Continuous Flow Electrophoresis in Perspective," *Phys. Chem. Hydrodyn.*, 1, 297 (1980).

Saville, D. A., and O. A. Palusinski, "Theory of Electrophoretic Separations. I: Formulation of a Mathematical Model," *AIChE J.*, 32, 207 (1986).

Tiselius, A., "A New Apparatus for Electrophoretic Analysis of Colloidal Mixtures," *Trans. Faraday Soc.*, 33, 524 (1937).

Watts, H. A., "Step Size Control in Ordinary Differential Equation Solvers," *Trans. Soc. Computer Simulation*, 1, 15 (1984).

Manuscript received June 26, 1984, and revision received Mar. 30, 1985.